Tip-Enhanced Near-Field Raman Scattering: Fundamentals and New Aspects for Molecular Nanoanalysis/Identification

Prabhat Verma[1], Yasushi Inouye[2,3], and Satoshi Kawata[1,3]

[1] Department of Applied Physics, Osaka University, Suita, Osaka 565-0871, Japan
[2] Graduate School of Frontier Biosciences, Osaka University, Suita, Osaka 565-0871, Japan
[3] RIKEN, Wako, Saitama, 351-0198, Japan
verma@ap.eng.osaka-u.ac.jp

1 Introduction

Raman scattering from molecules adsorbed on metallic nanostructures is strongly enhanced due to excitation of local surface-plasmon polaritons (SPPs). This gives rise to the well-known surface-enhanced Raman scattering (SERS) effect when the sample is dispersed on a rough metallic surface. Even a single metallic nanostructure, e.g., a metallic nanosized needle tip, can induce SERS at the tip apex. Raman scattering enhanced by such a tip is called tip-enhanced Raman scattering (TERS). The essential feature of TERS utilizing an apertureless metallic tip is the use of the incident electric-field-enhancement effect at the proximity of the metallic tip apex. The most important feature that makes TERS so attractive is its capability of optical sensing with high spatial resolution beyond the diffraction limits of light. We have demonstrated enhancement with high spatial resolution in TERS measurements for several nanomaterials [1, 2, 3, 4, 5], using a metallic probe tip.

In this Chapter, we discuss some TERS results from different kinds of samples and show the nanoanalysis capabilities of this technique. In Sect. 2, we discuss briefly the localized SPPs at a metallic tip apex, followed in Sect. 3 by an introduction to the instrumentation utilized in the experiments. The TERS measurements on carbon nanotubes and rhodamine R6 are discussed in Sect. 4 and Sect. 5, respectively. Section 6 discusses the TERS results for a DNA-based adenine molecules, including a discussion on the specific Raman band shifts that occurred by pressurizing adenine molecules by the tip. Finally, the tip-enhanced coherent anti-Stokes Raman scattering is discussed in Sect. 7, where we show an extremely high spatial resolution of 15 nm.

2 Localized Surface-Plasmon Polaritons at the Tip

Plasmons are defined as electromagnetic excitations coupled to the free charges of a conductive medium, and the surface-plasmon polaritons (SPPs)

K. Kneipp, M. Moskovits, H. Kneipp (Eds.): Surface-Enhanced Raman Scattering – Physics and Applications, Topics Appl. Phys. **103**, 241–260 (2006)

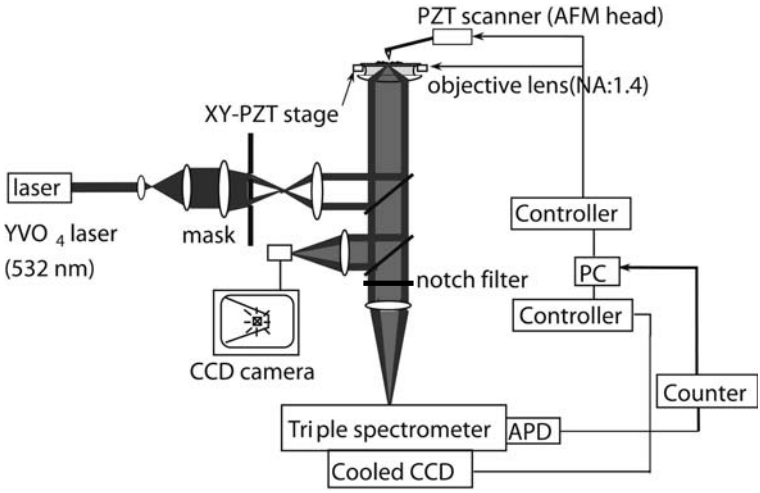

Fig. 1. Experimental setup for tip-enhanced near-field Raman spectroscopy

are such plasmons bound to an interface with a dielectric medium. Physically, one can understand it as photons coupled to collective excitations of conduction electrons on a metal surface. The speed of these SPPs is lower than the speed of light in the medium adjacent to the metal surface, so the electromagnetic field is evanescent or, in other words, these photons are non-propagative. Principally, SPPs can be excited in any kind of metal structure, but excitations in structures much smaller than the wavelength of the exciting light are distinguished by a pronounced resonance character. Such SPPs in the bounded geometry of a small structure are called the localized SPPs. These localized SPPs can be easily excited on small metallic structures and the incident light field is enhanced strongly. In the tip-enhanced near-field Raman scattering, a sharp apertureless metallic tip (e.g., a silver-coated AFM-cantilever tip) with a tip apex of about a few tens of nanometer is utilized as the small metallic structure to generate the localized SPPs. The electric field that is coupled to the localized SPPs at the apex of this metallic tip comprises an evanescent field. Since the evanescent field is localized around the tip apex, a super-resolution capability is attained by detecting this field. Therefore, an enhancement in the scattered field along with a super-resolution can be achieved by using a sharp metallic tip in TERS measurements.

3 Instrumentation

The basic difference in the instrumentation of micro-Raman spectroscopy (far-field detection) and the near-field TERS is related to the fact that in the former, Raman scattering is collected from all the sample molecules present in

the focal spot of the probing light, whereas in the latter, the Raman scattering cross sections of the sample molecules just below the enhanced electric field near the metallic tip apex are selectively enhanced and detected to provide a sufficiently high spatial resolution depending on the size of the enhanced electric field that corresponds to the diameter of the metallic tip, e.g., less than 30 nm. The experimental setup for the near-field TERS is shown in Fig. 1. An expanded and collimated light beam from a frequency-doubled YVO_4 laser (wavelength: 532 nm, power: 50 mW) enters into the epi-illumination optics. A circular mask is inserted in the beam path of the illumination light and is located at the conjugate plane of the pupil of the objective lens with a numerical aperture (NA) equal to 1.4. This mask rejects part of the beam corresponding to focusing angles that are less than NA = 1.0, and the transmitted light is focused to produce an evanescent field on the sample surface [6]. As the metallic tip is moved into the focused spot, a highly *p*-polarized evanescent field excites surface-plasmon polaritons at the tip apex, and an enhanced electric field that is localized at the tip is generated [7, 8]. The localized enhanced electric field at the tip is scattered inelastically by the Raman-active molecules, which constitutes the near-field Raman scattering. The Raman scattering is collected by the same objective lens, and is directed to the triple-grating spectrophotometer operated in subtractive dispersion that is equipped with a liquid-nitrogen-cooled CCD camera for Raman spectra measurement and with an avalanche photodiode (APD) for Raman imaging. The APD is located after the exit slit of the spectrophotometer so that a specific Stokes-shifted line can be detected. The metallic tip is a commercial AFM silicon cantilever that is coated with a silver layer by a thermal evaporation process. The evaporation rate was adjusted to a relatively slow rate of 0.3 Å per second to avoid undesirable bending of the silicon tip. The silver-coated tip diameter was around 30 nm. The distance between the sample and the cantilever is regulated by contact-mode AFM operation, and the sample is scanned with piezoelectric transducers (PZT) in the X–Y plane. Scanning the XY-PZT sample stage while simultaneously detecting the Raman signal with the avalanche photodiode can perform near-field Raman imaging at the specific Stokes-shifted line.

Some additional features of the experimental setup utilized for CARS experiments are discussed further in Sect. 7.

4 TERS from Single-Wall Carbon Nanotube

Far-field Raman spectroscopy has recently been recognized as a very powerful tool to evaluate single-wall carbon nanotubes (SWNT) and it achieved an individual SWNT detection [9, 10] because much structural information including chirality and diameter could be deduced from the vibration modes [11]. To further detail the specific structure-dependent single-molecule property, a single-molecule addressing capability at the nanometer scale is needed,

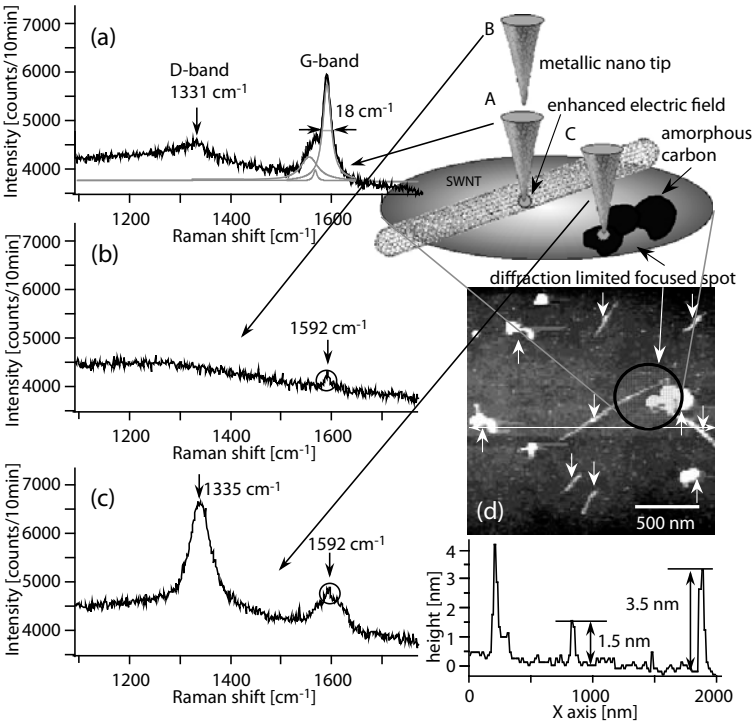

Fig. 2. (**a**) TERS spectra of an individual SWNT, which is obtained at the schematically shown tip position of "A". Remarkable tangential G-band peaks of SWNT and a small D-band peak at 1331 cm^{-1} are observed. The G-band peaks are well fitted by a Lorentzian lineshape at the peak positions of 1593 cm^{-1}, 1570 cm^{-1}, and 1558 cm^{-1} (*gray lines*). (**b**) Far-field Raman spectrum of SWNT with the tip being 500 nm away from the sample surface shown in "B". (**c**) TERS spectrum of an amorphous carbon, which is obtained at schematically shown tip position of "C". (**d**) Topographic AFM image and the cross section (*white line in the image*) of the isolated SWNTs dispersed on a coverslip. Some isolated SWNTs indicated by *downwards arrows* and amorphous carbon particles indicated by *upwards arrows* can be seen in the image. The dimension of the image is 2 μm × 2 μm consisting of 200 × 200 pixels

which can be provided by the TERS technique. For these measurements [3], we sparsely spread out SWNTs on a coverslip, and focus a laser beam at a tube (Fig. 2d). Generally, our sample consisted of bundles of SWNTs, however, after spincoating, some individual SWNTs could be separated out from aggregated bundles of SWNTs. Figure 2a shows a TERS spectrum of an individual SWNT, obtained at the schematically shown tip position "A". Remarkable tangential G-band peaks, representing a graphite mode, of a SWNT that is split into three peaks and fitted well to the Lorentzian lineshape at 1593 cm^{-1}, 1570 cm^{-1}, and 1558 cm^{-1} were observed (gray lines

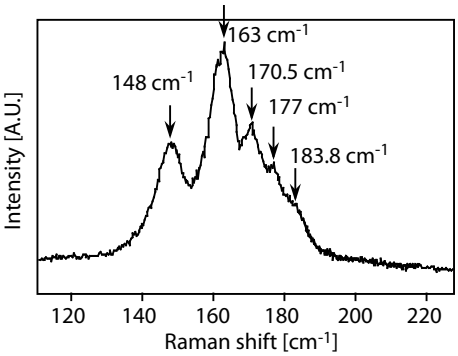

Fig. 3. High-resolution far-field Raman spectrum of radial breathing mode from aggregated bulk of SWNTs detected with a double-grating spectrometer

in Fig. 2a). These Lorentzian lineshapes feature semiconducting SWNTs, excluding the Breit–Wigner–Fano lineshape [12] that is observed in the resonant Raman spectra of metallic SWNTs. The fitted linewidth at 1593 cm^{-1} is 18 cm^{-1}. Taking into account that the FWHM of the excitation laser detected by our single spectrometer with an entrance slit width of 250 μm has a linewidth of 10 cm^{-1}, the deduced linewidth at 1593 cm^{-1} is 8 cm^{-1}. This narrow linewidth suggests that the observed isolated SWNTs consist of only one or a few SWNTs [13]. A small D-band peak, representing a defect mode, at 1331 cm^{-1} was also detected.

Due to the strong coupling between electrons and phonons in the resonant Raman effect, the unique one-dimensional electronic density of states of SWNTs plays an important role in the exceptionally strong resonant Raman spectra of SWNTs associated with the interband optical transitions between two van Hove singularities [14]. According to [15], while the 532 nm wavelength of our light source, carrying a photon energy of 2.33 eV, can resonantly excite electrons contained in semiconducting SWNTs whose diameter is from 1.35 nm to 1.55 nm, the optical absorption spectrum does not show the corresponding strong absorption [15]. However, the tip-enhancement effect compensates for this less efficient resonant Raman effect. Furthermore, the high-resolution far-field Raman spectrum detected with a double-grating spectrometer at the aggregated bulk of SWNTs included in the sample, shown in Fig. 3, can give us the diameter distribution of the SWNTs [16]. Five apparent peaks are detected as radial breathing modes. By using a simple approximation between mode frequency W_{RBM} (cm^{-1}) and the diameter d (nm), i.e., $W_{\mathrm{RBM}} = 224/d$ [11], the peaks of the radial breathing modes at 148 cm^{-1}, 163 cm^{-1}, 170.5 cm^{-1}, 177 cm^{-1}, and 183.8 cm^{-1} correspond to the diameters of 1.51 nm, 1.37 nm, 1.31 nm, 1.27 nm, and 1.22 nm, respectively. This diameter feature is also supported by the TERS spectrum of the radial breathing mode shown in Fig. 4. The spectra a–c in Fig. 4 correspond to

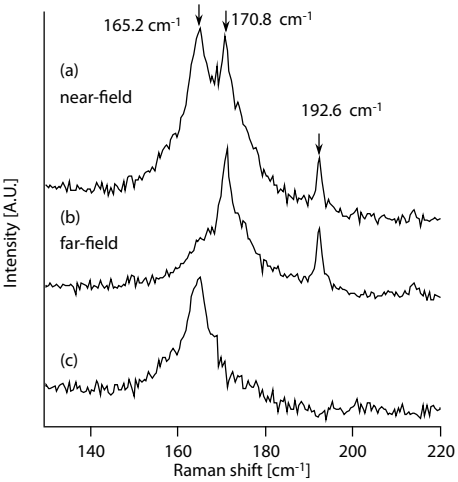

Fig. 4. (**a**) TERS and (**b**) far-field Raman spectra of radial breathing mode of isolated SWNTs. (**c**) The subtracted Raman spectra between far-field and TERS. The Raman peak at 165.2 cm^{-1} corresponding to the diameter of 1.50 nm is selectively enhanced by the metallic probe tip

tip-enhanced near-field, far-field, and the subtracted Raman spectra, respectively. The metallic probe tip selectively enhanced the SWNT just below the tip so that the enhanced Raman peak at 165.2 cm^{-1} is clearly observed, while other peaks such as 170.8 cm^{-1} and 192.6 cm^{-1}, which are generated from the far-field focused spot are not enhanced. By using the modified approximation for individual SWNTs, $W_{\mathrm{RBM}} = 248/d$ [9], the Raman peak at 165.2 cm^{-1} corresponds to the diameter of 1.50 nm. The topographic image of the sample (Fig. 2d) confirms the height of the SWNT (~ 1.5 nm) and clearly shows the distribution of SWNTs and amorphous carbon. This image was obtained in AFM operation by the tip-enhanced near-field microscope. The white lines in the figure indicated by downwards arrows are isolated SWNTs. The height of the observed isolated SWNT is ~ 1.5 nm corresponding to the diameter of an individual SWNT, while the other one has the height of 3.5 nm consisting of several SWNTs. White spots with a diameter of ~ 100 nm indicated by upwards arrows are amorphous carbon inherently included in our sample as the impurities of the arc-discharge process of SWNTs.

Accordingly, the most possible chirality for the semiconducting SWNT observed in the TERS spectrum is (17.4) $\sim$ 1.513 nm. Note that the peak at 192.6 cm^{-1} in Fig. 4 is not observable in the high-resolution far-field Raman spectra from the aggregated bulk of SWNTs in Fig. 3. This can be attributed to the fact that the number of SWNTs in Fig. 4 is extremely small compared to that of Fig. 3. The averaging effect overwhelmed the characteristic peak at 192.6 cm^{-1} in Fig. 3.

Figure 2b was obtained when the metallic probe tip was 500 nm away from the sample surface (the tip position of "B"). This spectrum represents a far-field Raman spectrum, where the featured lines are gone due to the absence of a field-enhancing metallic probe tip in the near-field except for a small protrusion at $1592\,\mathrm{cm}^{-1}$. Since the sample contains not only SWNTs but also impurities (amorphous carbon), this small peak represents an average within a focused spot of the laser beam, however, the spectrum dominantly reflects the non-enhanced G-band feature of SWNTs. Note that although isolated SWNTs are randomly dispersed and aligned parallel to the substrate, we can observe the G-band of isolated SWNTs only at several far-field focused positions by an objective lens, and the observed far-field Raman intensity at each position is different. Because of the polarization effect of both illumination light field and SWNTs and the severe selectivity of the resonant Raman effect [15], the number of observable isolated SWNTs is quite limited. These facts suggest that the observed isolated SWNT consists of only one or a few SWNTs. Figure 2c shows another TERS spectrum from the same sample when the probe enhances the field at a different location. A broad D-band representing the defect mode of amorphous carbon is dominantly detected around $1335\,\mathrm{cm}^{-1}$ [17]. The G-band is also seen but it is wider than that seen in Fig. 2a. This can be attributed to the tip position schematically shown by "C". A small G-band peak shown in Fig. 2b (circle in the figure) is recognizable on the top of the broad G-band peak in Fig. 2c (circle in the figure). The broad G-band peak represents the tip-enhanced near-field Raman scattering of amorphous carbon due to the tip, while the small G-band peak is the far-field background signal coming from an isolated SWNT. The sharp tangential G-band feature of an individual semiconducting SWNT (Fig. 2a) and the broad D-band and G-band feature of amorphous carbon (Fig. 2c) are explained on the basis that the enhanced electric field at the metallic probe tip selectively enhances the near-field Raman scattering of the SWNT and amorphous carbon inside of the tightly focused spot by the objective lens.

5 TERS Measurements on Rhodamine 6G

Rhodamine 6G (R6G) molecules dispersed on a silver-island film were studied by TERS and the corresponding spectra are shown in Fig. 5 [2, 18]. The TERS spectra a–d, h, and i together with spectrum j in Fig. 5 are quite similar to the far-field surface-enhanced resonant Raman scattering (SERRS) spectrum [18]. On the other hand, some of the spectra, such as the spectra e, f, and g in Fig. 5 exhibit anomalous spectral patterns that are different from those in the far-field SERRS [18]. Such anomalous spectral patterns, in detail, seem to have an overlap of several new peaks, in addition to the TERS spectral pattern analogous to the far-field SERRS. The frequencies of most TERS bands are found to be consistent with those of the SERRS peaks. In addition, the intensities of some TERS bands such as those at $702\,\mathrm{cm}^{-1}$, $1027\,\mathrm{cm}^{-1}$,

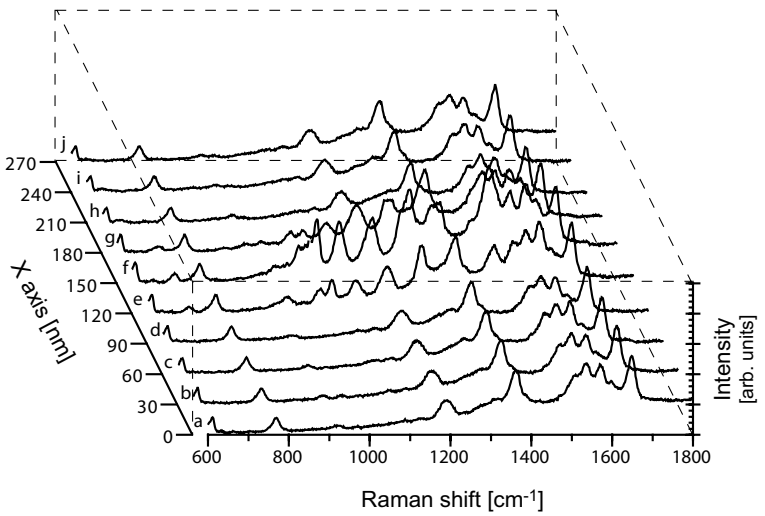

Fig. 5. TERS spectral mapping of R6G adsorbed on silver film at several positions. Labels a–j correspond to various tip positions where the TERS spectra were observed

1061 cm^{-1}, 1120 cm^{-1}, 1269 cm^{-1}, and 1457 cm^{-1} are quite inconsistent with those of the SERRS being strongly enhanced.

In the TERS spectra, such as spectra a–d, h, and i in Fig. 5, an averaged enhancement factor by the metallic tip is estimated from the TERS/SERRS signal ratio at 1647 cm^{-1} [4]. The averaged enhancement factor by the tip reaches approximately 1×10^2, which is extrapolated for the spot area (400 nm ϕ) from the metallic tip diameter (40 nm ϕ). Meanwhile, a specific enhancement factor is estimated from the signal ratio of the most strongly enhanced peak at 1054 cm^{-1} in spectrum f. The specific enhancement factor reaches approximately 2×10^4. In TERS spectroscopy, enhancement mechanisms caused by the metallic tip are thought to be the same as the SERS, the electromagnetic (em), and the charge transfer (CT). In addition to these SERS-like enhancement mechanisms, the third mechanism is proposed as a mechanical pressure mechanism due to molecular deformation by the tip [5]. According to the former two enhancement mechanisms, a ratio of the specific/averaged enhancement factors at least correspond to the contribution of the CT mechanism to the enhancement. The ratio obtained in the TERS experiment is less than or equal to 10^2; this magnitude is as much as a generally accepted degree of the enhancement effect caused by the CT mechanism [19, 20, 21].

The vibrating regions of all the peaks with anomalous TERS signal are located on the opposite side of the amino group that is bonded to the silver surface. The CT mechanism can be explained by the resonant Raman mechanism in which charge-transfer excitations (either from the metal to the

adsorbed molecule, or vice versa) occur at the energy of incident laser frequency [21]. In the case of the TERS, the electronic wavefunctions overlap between the silver atoms of the metallic tip apex and molecular orbitals of the adsorbed species is a requirement for the charge-transfer excitations. With an excitation frequency at 488 nm (2.54 eV), adsorbates such as R6G having a narrow HOMO–LUMO bandgap are electronically excited from the lower occupied orbitals to a Fermi level of silver surfaces, or from the Fermi level to higher virtual orbitals. In the R6G molecule, occupied orbitals (ϕ_{116} and ϕ_{117}) and a virtual orbital (ϕ_{120}) are the candidates for the CT electronic excitations in comparison with their energy differences from the Fermi level and the excitation frequency. An electron density distribution of the occupied orbitals (ϕ_{116} and ϕ_{117}) is localized in the xanthene ring, and that of the virtual orbital (ϕ_{120}) is centralized in the phenyl ring. In our Raman NSOM setup, the silver metallic tip approaches from the opposite direction toward the adsorbed R6G molecules on the silver-island film and touches the molecules by the contact mode of the AFM standard operation. As the silver atoms of the tip at the apex interact with the virtual orbital (ϕ_{120}) at the phenyl ring of the R6G molecules, the bands due to symmetric deforming motions of the phenyl ring could be highly enhanced in their TERS intensities. Hence, the specific intensity enhancement of some of these TERS bands could be understood with the CT mechanism caused by the silver tip together with the approaching direction of the tip toward the molecule. From the viewpoint of the molecular orientations, it is strongly suggested that R6G molecules in the anomalous regions turn the opposite part of the molecules against the adsorption site to the direction of the metallic tip. In other words, the R6G molecules are in a state of higher order such as assembly or aggregation in the anomalous regions.

Comparing the enhancement factors of SERRS/RRS and TERS/SERRS, the averaged enhancement factor of TERS/RRS and the factor at the specific band are estimated to be approximately 1×10^6 and 2×10^8, respectively. In particular, the enhancement factor at the specific band is beyond the values that are usually obtained in the conventional SERS measurement. Recent progress in single-molecule detection of SERS reveals that a gigantic local plasmonic field is generated at a junction between two connecting metallic nanoparticles [22, 23]. In our TERS system, R6G molecules are tightly sandwiched between the silver-island film (thickness = 8 nm) and the silver tip (40 nm ϕ) by the contact mode of the AFM. These contacting areas could be the junctions (hot spots). Supposing that the hot spot is an area where all particles (40 nm ϕ) are contacting within a gap of 1 nm, the diameter of the hot-spot area would be less than 1 nm on the basis of the finite difference time-domain (FDTD) method [23, 24]. Accordingly, the enhancement factor at the specific band would reach the 10^{11} to 10^{12} level, which is estimated for the conventional TERS observable area by the area of the hot spot. This means a metallic tip surface doubly enhanced Raman scattering has a possibility to detect the molecular vibration of subnanometer size at the level of

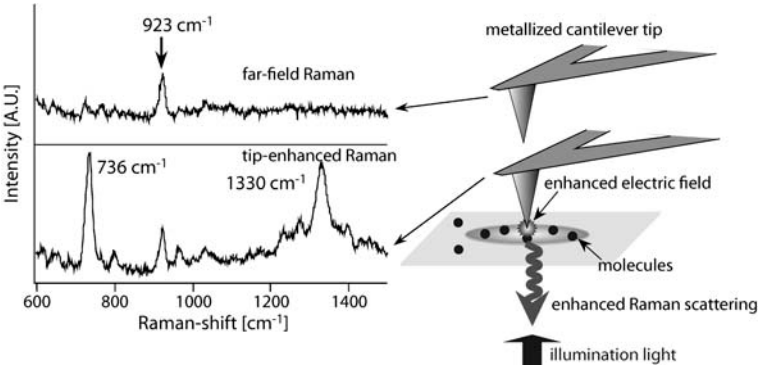

Fig. 6. Tip-enhanced near-field Raman (*lower spectrum*) and far-field Raman (*upper spectrum*) spectra of adenine nanocrystals. The peak at $923\,\mathrm{cm}^{-1}$ is from the glass substrate, and shows the same intensity both in TERS and the far-field Raman spectra. A schematic of the tip position in the two cases is also shown

a single molecule. Under such a strong electric field, two enhancement mechanisms would be tentatively considered. One is an extended CT mechanism where the bands of SERRS-inactive vibrational modes could be enhanced either with a vibronic coupling (the Albrecht B term [25]) or with electronic excitations that are not excited by the classical, linear CT mechanism. Another is a polarized em mechanism where Raman bands could be enhanced by a highly polarized electric field coupled with their Raman polarizability tensors. Intensity fluctuation of specific vibrational modes of R6G was reported in the single-molecule Raman detection [5, 26], and the calculated polarizability tensors of the specific Raman bands of the R6G molecule are parallel to the approaching direction of the tip.

6 Tip Force on DNA-Based Adenine Molecules

In this section, we will first discuss the normal TERS results from a DNA-based adenine molecule and demonstrate how the metallic tip enhances the weak Raman signal from a nanometer region, which cannot be detected by a conventional micro-Raman configuration. In the next part, we will show the effect of pressure that a tip can apply on the sample during the TERS experiments.

6.1 TERS from Adenine

Adenine nanocrystals are spread out on a coverslip by casting adenine molecules dissolved in ethanol [3]. The crystal size is laterally $7\,\mathrm{nm} \times 20\,\mathrm{nm}$ wide and 15 nm high. Figure 6 shows a TERS spectrum of a single nanocrystal

of adenine molecules. For a comparison, a far-field Raman spectrum of the same sample without a metallic tip is also shown. Figure 6 also schematically shows the tip position in the two cases. In the TERS spectrum, several characteristic Raman peaks of adenine molecules are enhanced and become visible, such as peaks at $736\,\mathrm{cm}^{-1}$ and $1330\,\mathrm{cm}^{-1}$, while no Raman peak at these positions is observed when the tip is withdrawn from the near-field region (far-field Raman spectrum). The experimental condition was exactly the same for both experiments shown in Fig. 6 except for the tip–sample distance. The strong Raman peaks at $736\,\mathrm{cm}^{-1}$ and $1330\,\mathrm{cm}^{-1}$ are assigned to ring–breathing mode of a whole molecule and the ring-breathing mode of a diazole, respectively. Other Raman peaks are also assigned to the normal modes of adenine molecules [27, 28, 29]. The observed TERS peaks are shifted slightly from those obtained in the far-field. For example, the ring-breathing mode at $720\,\mathrm{cm}^{-1}$ in the far-field Raman spectrum of the bulk sample is shifted to $736\,\mathrm{cm}^{-1}$ in the TERS spectrum, while the ring-breathing mode of a diazole is not shifted. These phenomena in the spectral shifts are in good agreement with the SERS spectra of adenine molecules [30], and ensure that the metallic probe tip works as a surface enhancer for the SERS effect.

Assuming that the enhanced electric field is 30 nm ϕ corresponding to the tip diameter and the focused light spot is 400 nm ϕ, the enhancement factor for the ring-breathing mode of a whole molecule is 2700. Furthermore, the factor for the ring-breathing mode of a diazole is uncountable because the far-field Raman signal without a metallic probe tip is too weak to be detected.

6.2 TERS from Tip-Pressurized Adenine Molecules

One of the major differences in the experimental conditions between the TERS from those of the SERS is the interaction mechanism of adenine with silver surfaces. In SERS, adenine is adsorbed in equilibrium onto silver surfaces and it interacts with the silver atoms electromagnetically and chemically. However, in TERS, apart from these two interactions, the tip and the sample can also interact mechanically, if the metal molecules of the tip push against the sample molecules. This effect can be observed if the sample is pressurized, intentionally or unintentionally, by the tip [5]. Unlike the isotropic hydraulic pressure usually studied in high-pressure Raman scattering [31, 32, 33], the pressure applied by a tip is unidirectional, and hence it can change the bond lengths uniaxially, resulting in modifications of the molecular vibrations. The Raman modes tend to shift and get broadened. Assuming that the atomic force is applied only to the contraction of the bond between the silver atom of the tip and the adjacent nitrogen of the adenine molecule, the bond distance would be expected to shrink and the vibrational frequencies may then shift upwards.

In our experiment, we used a cantilever with a spring constant of $0.03\,\mathrm{N/m}$ and a silver-coated tip apex diameter of this cantilever was 5 nm to 10 nm.

The atomic force was kept constant at 0.3 nN by the feedback loop. As deduced from the unit-cell parameters of single-crystal 9-methyladenine [34], a couple of adenine molecules exist in a rectangle approximately 0.77 nm long by 0.85 nm wide. If we assume that the force is equally applied to all the molecules that are adjacent to the tip apex, the adenine molecules are subjected to a pressure of ~ 1 to 5 pN per molecule by the silver atom attached on the surface of the tip. As the metallic tip approaches the surface of the adenine nanocrystal, the tip is at first subject to a van der Waals attractive force and after passing through the equilibrium point, the tip receives a repulsive force. When the bond distance of the Ag–N linkage is reduced by 10 %, the repulsive force of 7 pN per molecule is derived from a harmonic oscillation of the displacement by 0.025 nm and the energy difference by 1.7 kcal/mol in the case of the Ad–N3. The repulsive force coincides with the atomic force obtained with our system.

For the further understanding of the tip-enhanced near-field Raman active species of adenine molecules, we theoretically investigated (using the density functional theory calculations) the transition states of both the Ad–N3 and the Ad–N7 isomers by changing the bond distance (in the model) between the nitrogen of the adenine molecule and the silver atom. The bond distances for the calculations were 2.502 (equilibrium), 2.75 (10 % elongation), 2.25 (10 % contraction), and 2.0 Å (20 % contraction). The binding energies, the vibrational frequencies of free adenine molecules, and the two complex isomers of three states are calculated. The partially optimized geometries exhibit imaginary frequencies, indicating transition states for the Ad–N3 and the Ad–N7. The ring–breathing mode of the Ad–N3 shows a significant shift towards a higher frequency as a function of the contracted bond distance between the silver atom and the N3 nitrogen of adenine. The frequency of this mode is shifted upwards by 5 cm^{-1} when the bond distance is reduced by 10 %. The frequency is shifted upwards by 17 cm^{-1} when the bond distance is reduced by 20 %. The frequency shift of this band agrees well with those obtained in TERS experiments. On the other hand, the Ad–N7 shows only small frequency shifts. This difference in frequency shift suggests that interaction between an adenine molecule and the silver tip (e.g., the Ad–N3) may be one of the possible reasons that we see large enhancement effects in TERS.

In addition to the higher-frequency shift, Raman-band broadening is also observed in TERS. The line broadening as well as the Raman frequency shift have also been reported in far-field high-pressure Raman scattering studies [31, 32, 33]. The line broadening occurs not only as a result of surface interaction, but also as a result of pressures caused by the silver tip.

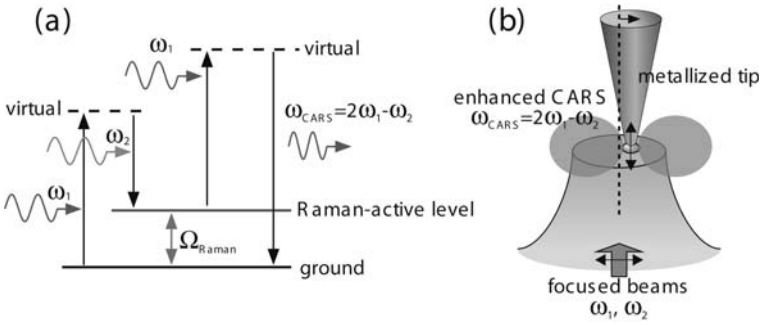

Fig. 7. (**a**) Energy diagram of coherent anti-Stokes Raman scattering process. (**b**) Tip enhancement of CARS polarization of molecules near the metallic tip in a tightly focused spot

7 Tip-Enhanced Coherent Anti-Stokes Raman Scattering

Coherent anti-Stokes Raman scattering (CARS) is one of the most powerful four-wave mixing spectroscopic methods, which includes a pump field (ω_1), a Stokes field (ω_2; $\omega_2 < \omega_1$), and a probe field (ω_1), and induces a nonlinear polarization at the frequency of CARS [35], as shown in Fig. 7a. When the frequency difference of ω_1 and ω_2 ($\omega_1 - \omega_2$) coincides with one of the specific molecular vibrational frequencies (Raman) of a given sample, the anti-Stokes Raman signal is resonantly generated. CARS spectroscopy is sensitive to molecular species and molecular conformation, resulting in a method of molecule identification without staining. As a CARS spectrum is obtained by scanning the frequency difference between two lasers, a high-resolution spectrometer is not required. Biological samples often have strong autofluorescence that overlaps that of Stokes-shifted Raman scattering. Since the frequency of CARS is higher than those of CARS excitation lasers, CARS emission is separable from fluorescence. Although CARS spectroscopy has the above-mentioned advantages, it has not been utilized for microscopy since the report of CARS microscopy by *Duncan* et al. in 1982 [36]. Phase matching is required for CARS, and consequently it was thought to be difficult that high spatial resolution consists with the phase-matching condition. Recently, CARS microscopy has been realized to have a three-dimensional resolving power by collinear illumination optics [37, 38], using a high-NA objective lens. In this case, the phase-matching condition is relaxed at the tightly focused light spot. CARS is generated only at the focal point in the sample medium, similar to two-photon fluorescence microscopy [39].

In order to circumvent the problems of extremely small signals in nanoscaled spectroscopic sensing, we have proposed a combination of a third-order nonlinear optical effect with the field-enhancement effect of a metallic tip, that is, a technique for vibrational nanoimaging with tip-enhanced coher-

ent anti-Stokes Raman scattering (TE-CARS), one of third-order coherent nonlinear Raman scattering [35]. The alternative type of NSOM using an aperture-type probe was previously combined with CARS spectroscopy by *Schaller* et al. [40], where they employed a fiber probe for the signal collection of CARS excited by an external illumination and demonstrated chemical selective imaging of a biological specimen. The use of the tip-enhancement effect is, however, more advantageous with respect to spatial resolution, and is indispensable for observation of small numbers of molecules. The excitation of CARS polarization can be further confined spatially and highly enhanced at the very end of the probe tip owing to its third-order nonlinearity, providing higher spatial resolution than tip-enhanced spontaneous Raman scattering. We realized TE-CARS imaging of a specific vibrational mode of DNA molecules in the fingerprint region with a spatial resolution beyond the diffraction limit of light.

Recently, several scientists have reported that tight focusing of the excitation fields with a high-NA objective lens can achieve CARS microscopy with three-dimensional imaging capability at a submicrometer scale [37, 38]. The phase-matching condition can be satisfied automatically in the focused fields of multiple angles [41]. In other words, the phase-matching condition is not necessary to be considered when the CARS polarizations are generated only in a volume smaller than the propagation wavelength of CARS light [42, 43]. In our previous work, CARS was strongly amplified by isolated gold nanoparticles, which verified the possibility of the local enhancement of CARS by a metallic nanostructure [44]. Based on the concept mentioned above, one can observe CARS signals generated by the enhanced electric field at a metallic tip end of nanometric scale [45]. Figure 7b shows a schematic illustration of CARS generation by a metallic probe tip. Both the incident fields (ω_1 and ω_2) are strongly amplified by the metallic tip in the tightly focused spot, and induce CARS polarization with $\omega_{\mathrm{CARS}} = 2\omega_1 - \omega_2$ in the molecules located near the tip. As the z-polarized component of the electric field along the tip axis is dominant in the tip-enhanced field [46], the CARS polarizations are induced along the z-direction. For effective coupling of incident fields and tip-enhanced fields, the tip has to be in a position where the incident electric field in the z-direction is strong. Since we use linearly polarized beams, the peaks of the z-component are found at 200 nm from the center of the focused spot in the direction parallel to the polarization of the incident fields. Thus, the tip is displaced to one of the peaks, as shown in Fig. 7b. The CARS polarization of molecules is locally generated within the very small volume near the tip so that the ensemble of the induced polarizations behaves as a dipole oscillating in the z-direction, as seen in Fig. 7b. The backscattered component of the radiation can be efficiently collected with the high-NA focusing lens. Scanning the sample stage, while keeping the tip at the focused spot, can acquire two-dimensional TE-CARS images of a specific vibrational mode with a high spatial resolution that is determined by the size of the tip end rather than the diffraction-limited focused spot.

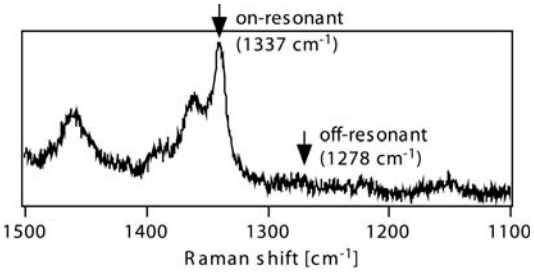

Fig. 8. A spontaneous Raman spectrum of the DNA of poly(dA-dT)-poly(dA-dT). The two frequencies adopted for our TE-CARS imaging are indicated by the *downward arrows*. The on-resonant frequency at $1337\,\mathrm{cm}^{-1}$ can be assigned to the ring-breathing mode of diazole adenine molecule in the DNA

The experimental setup mainly consists of two mode-locked Ti:sapphire lasers (pulse duration 5 ps, spectral band width $\sim 4\,\mathrm{cm}^{-1}$, repetition rate: 80 MHz), an inverted optical microscope, and an AFM using a silicon cantilever tip coated with a 20 nm thick silver film [1, 2, 3]. The ω_1 and ω_2 beams are collinearly overlapped in time and space, and introduced into the microscope with an oil-immersion objective lens (NA = 1.4) focused onto the sample surface. The AFM-controlled tip contacts the sample surface with a constant force and is illuminated by the focused spot. The repetition rate of the excitation lasers is controlled by an electro-optically (EO) modulated pulse picker. The backscattered CARS emission is collected with the same objective lens and detected with an APD based photon-counting module through an excitation-cut filter and a monochromator. The observing spectral width through the detection system is $\sim 12\,\mathrm{cm}^{-1}$. The pulse signals from the APD are counted by a gated photon counter synchronously triggered with the pulse picker. The dark counts are effectively reduced to ~ 0 counts/s with the gate width of 5 ns. The repetition rate was reduced to 800 kHz to avoid the thermal damage on both the sample and the silver tip while keeping the peak power high.

We used DNA molecules of poly(dA-dT) aggregated into clusters for TE-CARS imaging. The poly(dA-dT) solution in water (250 µg/ml) was cast and dried on a coverslip at room temperature with the fixation time of ~ 24 h. The dimensions of the clusters were typically ~ 20 nm in height and ~ 100 nm in width. The frequency difference of the two excitation lasers for TE-CARS was set to be $1337\,\mathrm{cm}^{-1}$, corresponding to a Raman mode of adenine (ring-breathing mode of diazole) by tuning the excitation frequencies ω_1 and ω_2 to be $12\,710\,\mathrm{cm}^{-1}$ (λ_1: 786.77 nm) and $11\,373\,\mathrm{cm}^{-1}$ (λ_2: 879.25 nm), respectively. After the "on-resonant" imaging, the frequency of ω_2 was changed such that the frequency difference corresponds to none of the Raman-active vibrations ("off-resonant"). Figure 8 shows a spontaneous Stokes Raman spectrum of the DNA in a part of the fingerprint region. The solid arrows on the spec-

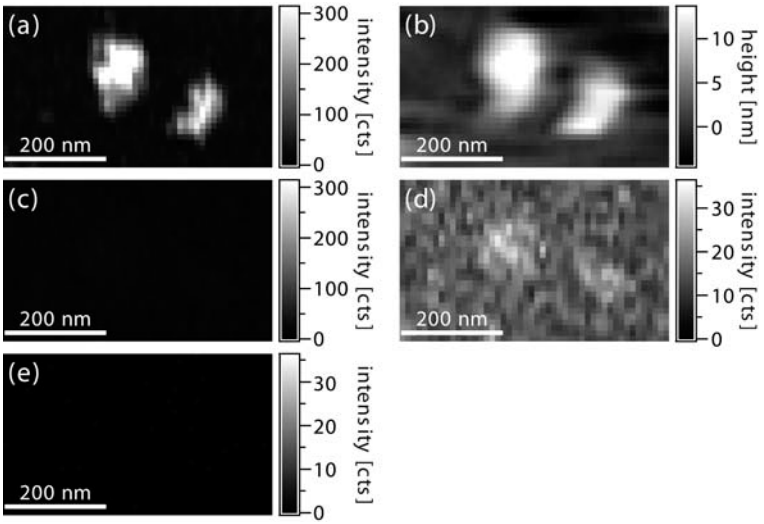

Fig. 9. TE-CARS images of the DNA clusters. (**a**) TE-CARS image at on-resonant frequency ($1337\,\mathrm{cm}^{-1}$), and (**b**) the simultaneously obtained topographic image. (**c**) TE-CARS image at the off-resonant frequency ($1278\,\mathrm{cm}^{-1}$). (**d**) The same image as (**c**) shown with a different gray scale. (**e**) Far-field CARS image of the corresponding area obtained without the silver tip. The scanned area is 500 nm by 300 nm. The number of photons counted in 100 ms was recorded for one pixel. The acquisition time was ~ 3 min for the image. The average powers of the 1 and 2 beams were $30\,\mu\mathrm{W}$ and $15\,\mu\mathrm{W}$ at the 800 kHz repetition rate

trum denote the frequencies adopted for the "on-resonant" and "off-resonant" conditions in TE-CARS imaging.

Figure 9 shows the TE-CARS images of the DNA clusters obtained by the TE-CARS microscope. Figures 9a and b are the TE-CARS image at the on-resonant frequency ($1337\,\mathrm{cm}^{-1}$) and the simultaneously acquired topographic AFM image. The DNA clusters of ~ 100 nm diameter are visualized in Fig. 9a. The two DNA clusters with a distance of ~ 160 nm are obviously distinguished by the TE-CARS imaging. This indicates that the TE-CARS imaging successfully achieved a super-resolving capability beyond the diffraction limit of light. At the off-resonant frequency ($1278\,\mathrm{cm}^{-1}$), the CARS signals mostly vanished in Fig. 9c. Figures 9a and c verify that vibrationally resonant CARS is emitted from the DNA molecules at the specific frequency. However, there remains some slight signal increase at the clusters at the off-resonant frequency, as seen in Fig. 9d, which is the same as Fig. 9c but is shown with a different gray scale. This can be caused by both the frequency-invariant (nonresonant) component of the nonlinear susceptibility of DNA [35] and the topographic artifact [47]. Figure 9e is the far-field CARS image at the on-resonant frequency, which was obtained after removing the tip from the sample. The CARS signal was not detected in the far-field CARS

image, which confirms that the CARS polarization is effectively induced by the tip-enhanced field. It can be noted that there exists background light in the presence of the tip, as is obvious from Fig. 9d. This background light is emitted from the silver-coated tip. The tip emits light at the same frequency as the CARS ($2\omega_1 - \omega_2$) by the third-order nonlinear susceptibility of silver, which is attributed to local four-wave mixing. In addition, noble metals such as gold and silver generate a white-light continuum, which is induced by multiphoton excited photoluminescence due to recombination radiation between electrons near the Fermi level and photoexcited holes in the d band [48, 49]. These two components become background light and compete with the CARS process. In our experiments the dominant background source is the FWM emission as the monochromator was utilized to selectively detect the signal at $2\omega_1 - \omega_2$. The background light can be seen at both the on-resonant and off-resonant frequencies, as they are independent of the molecular vibrations of the sample. Such light emission from a metallic tip degrades the image contrast and signal-to-noise ratio, and subsequently limits the smallest number of molecules that can be observed. In this experiment, however, the TE-CARS signal intensity largely surpasses the background because the number of molecules in the excited volume is enough to induce the signal.

In order to assess the capability of the sensitivity of the TE-CARS microscopy, we prepared a DNA network of poly(dA-dT)-poly(dA-dT) [50]. DNA (poly(dA-dT)-poly(dA-dT)) dissolved in water (250 μg/ml) was mixed with $MgCl_2$ (0.5 mM) solution, then the DNA solution was cast on a coverslip and blow-dried after the fixation time of $\sim$ 2 h. Mg^{2+} has a role for the linkage between DNA and oxygen atoms of the glass surface. Figure 10a shows a typical topographic image of the DNA network sample. The DNA network consists of bundles of DNA double-helix filaments aligned parallel on the glass substrate. Since the diameter of single DNA double-helix filaments is $\sim$ 2.5 nm, the height of the bundle structures is $\sim$ 2.5 nm, and the width is from 2.5 nm (for single filaments) to a few tens of nanometer (for ca. 10 filaments). The TE-CARS images at the on- and off-resonant frequencies are shown in Figs. 10b,c. The DNA bundles are observed at the resonant frequency in Fig. 10b, while they cannot be visualized at the off-resonant frequency in Fig. 10c. This indicates that the observed contrast is dominated by the vibrationally resonant CARS signals. Figure 10d shows one-dimensional line profiles at $y = 270$ nm, which were acquired with a step of $\sim$ 5 nm. The line profile of far-field CARS acquired without the silver tip is also added for comparison. Only the TE-CARS in the on-resonant condition has peaks at the positions of $x \sim 370$ nm and $x \sim 700$ nm where adenine molecules exist in the DNA double helix, while the other line profiles do not sense the existence of the molecules. The full width at half maximum of the peak at $x \sim 700$ nm is 15 nm, which confirms that with the existing TE-CARS setup, we are able to obtain a spatial resolution down to 15 nm. This extremely high resolution is attributed to the combination of the near-field effects of TERS and the nonlinearities of CARS. The intensity enhancement factor for

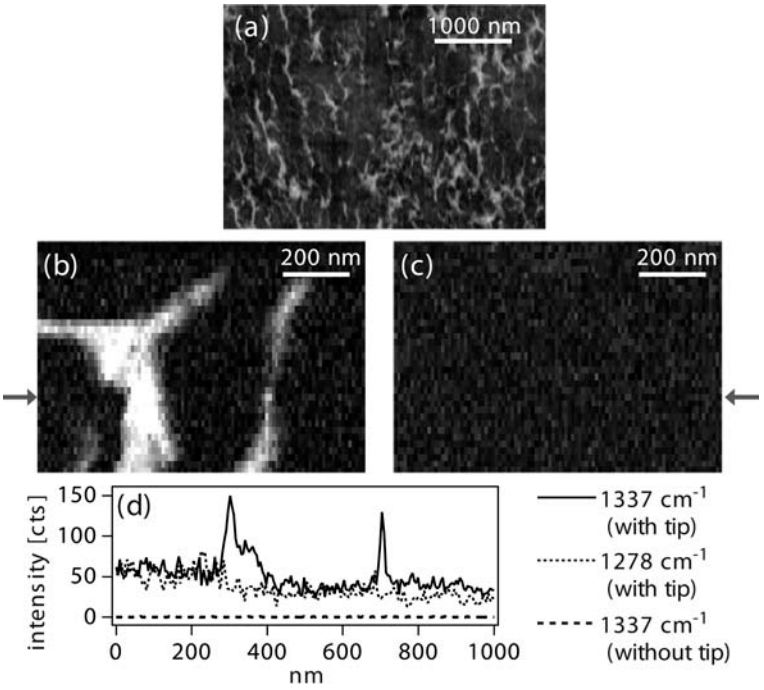

Fig. 10. TE-CARS images of the DNA network. (**a**) Topographic image of the DNA network. (**b**) TE-CARS image at on-resonant frequency ($1337\,\mathrm{cm}^{-1}$). (**c**) TE-CARS image at the off-resonant frequency ($1278\,\mathrm{cm}^{-1}$). (**d**) Cross-sectional line profiles of $y = 270\,\mathrm{nm}$ (indicated by the *solid arrows*). The scanned area is 1000 nm by 800 nm. The number of photons counted in 100 ms was recorded for one pixel. The acquisition time was $\sim 12\,\mathrm{min}$ for the image. The average powers of beams 1 and beam 2 were $45\,\mu\mathrm{W}$ and $23\,\mu\mathrm{W}$ at the 800 kHz repetition rate

each electric field is estimated to be $\sim$ 100-fold. The estimated value of the enhancement factor ($\sim$ 100) is quite realistic and reasonable, as compared to previous numerical results [8, 51], although this estimation is very much subject to the changes in each parameter with high-order dependency. We also estimated the size of the locally excited volume of the DNA structure to be $\sim$ 1 zeptoliter. The smallest detectable volume of DNA under the current experimental condition is estimated as $\sim \frac{1}{4}$ zeptoliter, which is derived from the signal-to-noise ratio of $\sim$ 15 : 1 in Fig. 10d and the quadratic dependence of the CARS intensity on interaction volume. This indicates that our TE-CARS microscope is capable of sensing a vibrational-spectroscopic signal from an extremely small subzeptoliter volume.

References

[1] N. Hayazawa, Y. Inouye, Z. Sekkat, et al.: Opt. Commun. **183**, 333 (2000)
[2] N. Hayazawa, Y. Inouye, Z. Sekkat, et al.: Chem. Phys. Lett. **335**, 369 (2001)
[3] N. Hayazawa, T. Yano, H. Watanabe, et al.: Chem. Phys. Lett. **376**, 174 (2003)
[4] N. Hayazawa, Y. Inouye, Z. Sekkat, et al.: J. Chem. Phys. **117**, 1296 (2002)
[5] H. Watanabe, Y. Ishida, N. Hayazawa, et al.: Phys. Rev. B **69**, 155418 (2004)
[6] N. Hayazawa, Y. Inouye, S. Kawata: J. Microsc. **194**, 472 (1999)
[7] S. Kawata: *Near-Field Optics and Surface Plasmon Polaritons* (Springer Berlin 2001)
[8] H. Furukawa, S. Kawata: Opt. Commun. **148**, 221 (1998)
[9] A. Jorio, R. Saito, J. H. Hafner, et al.: Phys. Rev. Lett. **86**, 1118 (2001)
[10] G. S. Duesberg, I. Loa, M. Burghard, et al.: Phys. Rev. Lett. **85**, 5436 (2000)
[11] M. S. Dresselhaus, P. C. Eklund: Adv. Phys. **49**, 705 (2000)
[12] S. D. M. Brown, A. Jorio, P. Corio, et al.: Phys. Rev. B **63**, 155414 (2001)
[13] K. Kneipp, H. Kneipp, P. Corio, et al.: Phys. Rev. Lett. **84**, 3470 (2000)
[14] R. Saito, M. Fujita, G. Dresselhaus, et al.: Appl. Phys. Lett. **60**, 2204 (1992)
[15] H. Kataura, Y. Kumazawa, Y. Maniwa, et al.: Synth. Met. **103**, 2555 (1999)
[16] A. M. Rao, E. Richter, S. Bandow, et al.: Science **275**, 187 (1997)
[17] F. Tuinstra, J. L. Koenig: J. Chem. Phys. **53**, 1126 (1970)
[18] H. Watanabe, N. Hayazawa, Y. Inouye, et al.: J. Phys. Chem. B **109**, 5012 (2005)
[19] M. Moskovits: Rev. Mod. Phys. **57**, 783 (1985)
[20] A. Otto, I. Mrozek, H. Grabhorn, et al.: J. Phys.: Condens. Matter **4**, 1143 (1992)
[21] A. Campion, P. Kambhampati: Chem. Soc. Rev. **27**, 241 (1998)
[22] A. M. Michaels, M. Nirman, L. E. Brus: J. Am. Chem. Soc. **121**, 9932 (1999)
[23] M. Futamata, Y. Maruyama, M. Ishikawa: J. Phys. Chem. B **107**, 7607 (2003)
[24] Y. Inouye, S. Kawata: Opt. Lett. **19**, 159 (1994)
[25] A. C. Albrecht: J. Chem. Phys. **34**, 1476 (1961)
[26] U. C. Fischer, D. W. Pohl: Phys. Rev. Lett. **62**, 458 (1989)
[27] A. D. Becke: J. Chem. Phys. **98**, 5648 (1993)
[28] C. Lee, W. Yang, R. G. Parr: Phys. Rev. B **37**, 785 (1988)
[29] M. J. Frisch, G. W. Trucks, H. B. Schlegel, et al.: computer code GAUSSIAN98 Revision A.9 (1998)
[30] C. Otto, T. J. J. van den Tweel, F. F. M. de Mul, et al.: J. Raman Spectrosc. **17**, 289 (1986)
[31] J. R. Ferraro: *Vibrational Spectroscopy at High External Pressures* (Academic, New York 1984) p. 2
[32] R. A. Crowell, E. L. Chronister: Chem. Phys. Lett. **195**, 602 (1992)
[33] S. A. Hambir, J. Franken, D. E. Hare, et al.: J. Appl. Phys. **81**, 2157 (1997)
[34] K. Hoogsten: Acta Crystallogr. **12**, 822 (1959)
[35] Y. R. Shen: *Principle of Nonlinear Optics* (Wiley, New York 1984)
[36] M. D. Duncan, J. Reintjes, T. J. Manuccia: Opt. Lett. **7**, 350 (1982)
[37] A. Zumbusch, G. R. Holtom, X. S. Xie: Phys. Rev. Lett. **82**, 4142 (1999)
[38] M. Hashimoto, T. Araki, S. Kawata: Opt. Lett. **25**, 1768 (2000)
[39] W. Denk, J. H. Strickler, W. W. Webb: Science **248**, 73 (1990)
[40] R. D. Schaller, J. Ziegelbauer, L. F. Lee, et al.: J. Phys. Chem. B **106**, 8489 (2002)

[41] M. Hashimoto, T. Araki: J. Opt. Soc. Am. A **18**, 771 (2001)
[42] J.-X. Cheng, A. Volkmer, X. S. Xie: J. Opt. Soc. Am. B **19**, 1363 (2002)
[43] Z. Xiaolin, R. Kopelman: Ultramicrosc. **61**, 69 (1995)
[44] T. Ichimura, N. Hayazawa, M. Hashimoto, et al.: J. Raman Spectrosc. **34**, 651 (2003)
[45] T. Ichimura, N. Hayazawa, M. Hashimoto, et al.: Phys. Rev. Lett. **92**, 220801 (2004)
[46] A. Bouhelier, M. Beversluis, A. Hartschuh, et al.: Phys. Rev. Lett. **90**, 013903 (2003)
[47] B. Hecht, H. Bielefeldt, Y. Inouye, et al.: J. Appl. Phys. **81**, 2492 (1997)
[48] G. T. Boyd, Z. H. Yu, Y. R. Shen: Phys. Rev. B **33**, 7923 (1986)
[49] J. P. Wilcoxon, J. E. Martin: J. Chem. Phys. **108**, 9137 (1998)
[50] S. Tanaka, L. T. Cai, H. Tabata, et al.: Jpn. J. Appl. Phys. **116**, L407 (2002)
[51] J. T. Krug II, E. J. Sánchez, X. S. Xie: J. Chem. Phys. **116**, 10895 (2002)

Index